Available online at www.sciencedirect.com
SCIENCE DIRECT®
International Journal of Heat and Mass Transfer 47 (2004) 1907–1916
International Journal of HEAT and MASS TRANSFER
www.elsevier.com/locate/ijhmt

Heterogeneous thermochemical decomposition under direct irradiation

W. Lipinski [a], A. Steinfeld [a,b,*]

[a] Solar Process Technology, Paul Scherrer Institute, CH-5232 Villigen, Switzerland
[b] Department of Mechanical and Process Engineering, ETH-Swiss Federal Institute of Technology, CH-8092 Zürich, Switzerland

Received 24 February 2003; received in revised form 26 September 2003

Abstract

Radiative heat transfer within a chemical reacting system directly exposed to an external source of high-flux radiation is considered. The endothermic decomposition of $CaCO_3$(s) into CaO(s) and CO_2(g) is selected as the model heterogeneous reaction. Its interfacial kinetic parameters are determined by thermogravimetric measurements assuming a contracting geometry rate law and an Arrhenius temperature dependence law. Experimentation using an Argon arc as the radiation source was carried out in which powder samples were subjected to radiative power fluxes in the range 400–930 kW/m^2. Temperature distributions and reaction extent were recorded as a function of time. A 3D transient heat transfer model that links conduction–convection–radiation heat transfer to the chemical kinetics is formulated using wavelength and chemical composition dependent material properties and assuming the Rosseland diffusion approximation for the internal radiative transport. Monte-Carlo ray tracing is employed to obtain the radiative flux distribution at the boundaries. The unsteady energy equation is solved by finite volume technique. The model is validated by comparing the computed temperature and reaction extent variation with time to the values experimentally measured.

1. Introduction

High-temperature endothermic chemical processes involving solid and gases are found in a wide range of industrial applications, including extractive metallurgy, ceramic material processing, and calcination. These processes are characterized by their high-energy consumption and the concomitant emission of pollutants, derived mainly from the combustion of fossil fuels for heat generation. The use of an external source of concentrated radiative energy for supplying the process heat offers several advantages, namely: (1) the products are not contaminated by combustion by-products; (2) heat is efficiently transferred by direct irradiation of reactants, bypassing the limitations imposed by indirect heat transport via heat exchangers; and (3) if the radiation source is derived from renewable energy, e.g. concentrated solar energy, the emission of greenhouse gases is avoided. Chemical reactors based on the concept of direct irradiation require matching the rate of radiation heat transfer to the rate of the chemical reaction. Modeling such an interaction is needed to anticipate the consequences of a given design decision on the reactor's performance.

The analysis of radiation heat transfer within a system undergoing a chemical transformation, in which the chemical species, phases, and system's properties vary with time as the reaction progresses, is a complex transient problem encountered in such research areas as combustion and atmospheric sciences. Examples of previous analyses that dealt with the steady-state approximation include a transport model for simulating vapor phase epitaxy growth based on the finite volume

* Corresponding author. Address: Department of Mechanical and Process Engineering, ETH-Swiss Federal Institute of Technology, ETH-Zentrum ML J42.1, CH-8092 Zürich, Switzerland. Tel.: +41-56-310-3124; fax: +41-56-310-3160.
E-mail address: aldo.steinfeld@eth.ch (A. Steinfeld).

0017-9310/$ - see front matter © 2003 Elsevier Ltd. All rights reserved.
doi:10.1016/j.ijheatmasstransfer.2003.10.010

Nomenclature

A	area, m^2
c_p	specific heat at constant pressure, $J\,kg^{-1}\,K^{-1}$
C_p	specific molar heat at constant pressure, $J\,mol^{-1}\,K^{-1}$
C_1	0.59552137×10^{-16} $W\,m^2\,sr^{-1}$
C_2	0.014387752 m K
E_a	apparent activation energy, $J\,mol^{-1}$
$e_{\lambda b}(T)$	spectral blackbody emissive power $=\frac{2\pi C_1}{\lambda^5(e^{C_2/(\lambda T)}-1)}$, $W\,m^{-2}\,\mu m^{-1}$
$F_{\lambda_1 T-\lambda_2 T}$	blackbody fractional function $=\frac{\int_{\lambda_1}^{\lambda_2} e_{\lambda b}(T)\,d\lambda}{\sigma T^4}$
g	power factor in the geometry rate law
h	convective heat transfer coefficient, $W\,m^{-2}\,K^{-1}$
H	height, m
k	reaction rate constant, s^{-1}
k_0	frequency factor, s^{-1}
k_c	thermal conductivity, $W\,m^{-1}\,K^{-1}$
k_r	Rosseland coefficient, $W\,m^{-1}\,K^{-1}$
K	extinction coefficient, m^{-1}
L	characteristic length, m
n	number of moles
$n_{0,CaCO_3}$	initial number of moles of $CaCO_3$
n_{CaCO_3}	actual number of moles of $CaCO_3$
M	molar mass, $kg\,mol^{-1}$
Nu	Nusselt number
N	number of particles per unit volume, m^{-1}
p	porosity
P	perimeter, m
Pr	Prandtl number
R	particle radius, m
Ra	Rayleigh number
q''	heat flux, $W\,m^{-2}$
q'''	heat generation rate per unit volume, $W\,m^{-3}$
q	heat generation rate, energy per unit time, W
t	time, s
T	temperature, K
u	specific internal energy, $J\,kg^{-1}$
U	internal energy per unit volume, $J\,m^{-3}$
V	volume, m^3
x	reaction extent

Greek symbols

α	thermal diffusivity, $m^2\,s^{-1}$
β	volumetric thermal expansion coefficient, K^{-1}
ΔH_T^o	standard reaction enthalpy change at temperature T, $J\,mol^{-1}$
Δx, Δy, Δz	spatial mesh size in x, y, and z directions, m
ε	emissivity
ζ	$C_2/\lambda T$
λ	wavelength, m
λ_c	wavelength cut-off for $CaCO_3$ and CaO, m
ν	kinematic viscosity, $m^2\,s^{-1}$
ρ	density, $kg\,m^{-3}$
σ	Stefan–Boltzmann constant $=5.67\times10^{-8}$ $W\,m^{-2}\,K^{-4}$
τ	transmissivity
Ω	finite volume

Subscripts

a	absorbed
air	air
c	conduction
ch	chemistry
cv	convection
e	emitted
in	incoming
interface	sample-plate interface
j	index of a cell
p	plate
p1, p2,...,p6	measurement points in the plate
r	radiation
reflected	reflected
s	sample
source	radiation source
t	top face of a cell
total	total flux
w	wall
λ	wavelength; spectral
τ	transmitted
0	initial value
∞	free stream value

Superscripts

n	time level
o	standard conditions
*	dummy variable
–	surface-averaged value

solution of coupled flow, heat, and mass transfer [1], a radiation transfer model coupled to the Navier–Stokes equations for a non-equilibrium medium existing in rocket exhaust plumes [2], and a radiative and convective heat transfer model coupled to the chemical kinetics of LPG reforming [3]. Examples of analyses that dealt with the transient problem include a two-phase model to predict ignition temperatures in an exothermic catalytic

chemical reactor [4], a 2D model of the ignition of polymethyl-methacrylate based on the discrete ordinates method [5], and a combined convection–conduction–radiation heat transfer model of an oil-fired furnace using the Hottel's zone and Monte-Carlo methods [6]. Chemical reactors for high-temperature thermochemical processes, in which the reactants are exposed to an external source of concentrated radiation, are found especially in solar chemical applications [7,8 and literature cited therein].

This paper presents an analysis of radiative heat transfer in a non-gray, non-isothermal solid undergoing heterogeneous thermochemical decomposition. A 3D model that couples the rate of radiative transfer to the chemical reaction kinetics is formulated, and the experimental set-up and measurements conducted for its validation are described.

2. Chemical kinetics

The thermal decomposition of limestone:

$$CaCO_3(s) = CaO(s) + CO_2(g) \tag{1}$$

is selected as the model reaction. The reaction proceeds endothermically at above 1200 K. Its enthalpy change, when the reactants are initially at 298 K and products obtained at 1200 K, is 270 kJ/mol. Thermogravimetric measurements were conducted with samples of mean particle size in the 2–3 mm range, at a heating rate of 10 K/min and air mass flow 100 ml/min. Applying a contracting geometry rate law [9],

$$\frac{dx}{dt} = k(1-x)^g \tag{2}$$

where x is the reaction extent, defined as $x = 1 - \frac{n_{CaCO_3}}{n_{0,CaCO_3}}$. The temperature dependency of k is determined by imposing the Arrhenius equation [9–11],

$$k = k_0 \exp\left(-\frac{E_a}{RT}\right) \tag{3}$$

The results are shown in Fig. 1 for $g = 0.5$. The apparent activation energy and frequency factor obtained by linear regression are $E_a = 187.3\ \mathrm{kJ\,mol^{-1}}$ and $k_0 = 6.45 \times 10^5\ \mathrm{s^{-1}}$, respectively.

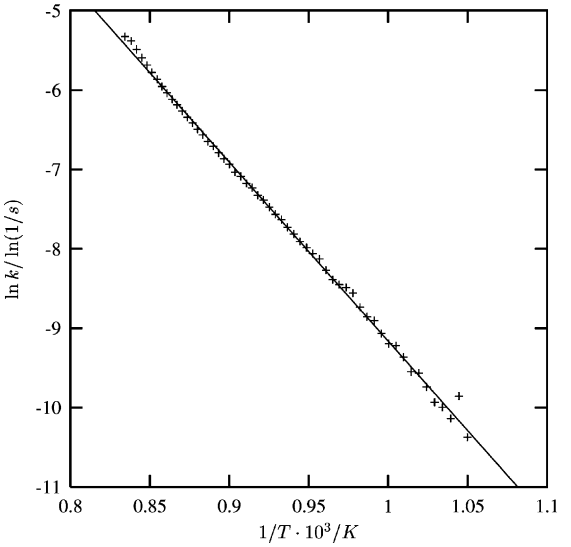

Fig. 1. Arrhenius plot for the thermal decomposition of $CaCO_3$: thermogravimetric measured values (data points) and linear regression using contracting geometry rate law.

3. Direct irradiation experimental set-up

Tests were conducted at the ETH's high-flux solar simulator [12]. This research facility provides a rapid external source of intense thermal radiation, mostly in the visible and IR spectrum [12]. It consists of a high-pressure argon arc enclosed in a 27 mm-diameter, 200 mm-length water-cooled quartz envelope. The light source is close-coupled to precision optical reflectors to produce an intense beam of concentrated radiant energy. The focusing mirrors are horizontal-axis troughs of elliptical cross section having a vertical major axis, and are positioned with one of the linear foci coinciding with the arc. The focal plane of the solar simulator is thus defined as the horizontal plane perpendicular to the ellipse's major axis containing the second linear focus. The elliptical mirrors are truncated 9.2 cm above the focal plane to permit external access, so that the reflected beam-down radiation is confined within an angular range of half-angle 45°. With this arrangement, power fluxes exceeding 4500 kW/m^2 are attained at the focal plane. Power, power fluxes, and temperatures can be adjusted to meet the specific requirements by simply varying the electrical input power to the arc electrodes. Power flux intensities are measured optically with an absolute point radiometer, with an estimated error of ±8%.

The experimental set-up is shown in Fig. 2. A 100 mm-length 20 mm-width 3.7 mm-height prism made of $CaCO_3$ particles was positioned on top of a 200 mm-length 148 mm-width 17 mm-depth refractory SiC plate, and mounted at the focal plane of the solar simulator. Thermocouples type-K were used to measure temperatures of the plate and plate-sample interface at various locations, as indicated in Fig. 2. Their exact location is listed in Table 1. Samples were irradiated at constant power fluxes during controlled intervals of time, weighted before and after each run to determine their mass loss, and finally completely calcined in an electrical

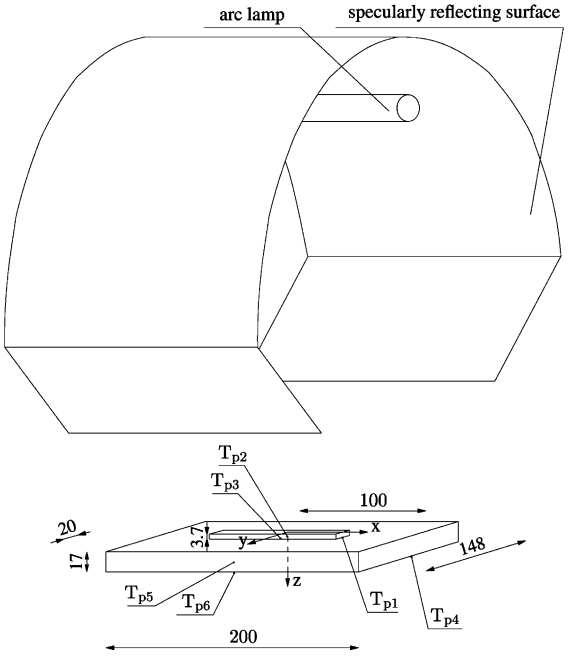

Fig. 2. Scheme and dimensions (in mm) of experimental set-up. Indicated are the positions of the temperature measurements and their corresponding notation.

Table 1
Location of temperature measurement points (see Fig. 2)

Measurement point	x/mm	y/mm	z/mm
T_{p1}	50	0	3.7
T_{p2}	0	0	3.7
T_{p3}	0	10	3.7
T_{p4}	100	0	20.7
T_{p5}	0	74	12.2
T_{p6}	0	74	20.7

furnace after each run to verify their degree of calcination.

4. Heat transfer model

The system domain is defined as the sum of two subsystems: the $CaCO_3$-prism sample plus the plate, as indicated in Fig. 2. Thus, the system is bounded by 11 planes. The general energy conservation law for a differential solid applied to each sub-system is given by [13]:

$$\frac{\partial U}{\partial t} = -\nabla \cdot \vec{q}'' + q''' \tag{4}$$

where U is the internal energy, q'' is the heat flux, and q''' is the heat sink/source per unit volume. For the sample, $U = \rho_{CaCO_3} u_{CaCO_3} + \rho_{CaO} u_{CaO}$, and for the plate, $U = \rho_{SiC} u_{SiC}$, u being the specific internal energy. The boundary conditions for the sample are:

- at the upper surface of the sample

$$-(1-p)k_{c,s}\frac{\partial T_s}{\partial n}\bigg|_w - pk_r\frac{\partial T_s}{\partial n}\bigg|_w = q''_e + q''_{cv} - q''_a \tag{5}$$

- at the sample-plate interface

$$-(1-p)k_{c,s}\frac{\partial T_s}{\partial n}\bigg|_w - pk_r\frac{\partial T_s}{\partial n}\bigg|_w = q''_{total,interface} \tag{6}$$

- at all other free surfaces of the sample

$$-(1-p)k_{c,s}\frac{\partial T_s}{\partial n}\bigg|_w - pk_r\frac{\partial T_s}{\partial n}\bigg|_w = q''_e + q''_{cv} \tag{7}$$

The boundary conditions for the plate are:

- at the upper free surface of the plate

$$-k_{c,p}\frac{\partial T_p}{\partial n}\bigg|_w = q''_e + q''_{cv} - q''_a \tag{8}$$

- at the plate-sample interface

$$k_{c,p}\frac{\partial T_p}{\partial n}\bigg|_w = q''_{total,interface} + q''_\tau \tag{9}$$

- at all other free surfaces of the plate

$$-k_{c,p}\frac{\partial T_p}{\partial n}\bigg|_w = q''_e + q''_{cv} \tag{10}$$

The set of boundary and initial conditions is closed by setting the free stream temperature around the system T_∞, and the initial temperature within the system T_0.

We now proceed to the derivation of the heat fluxes by radiation, convection, and conduction for each subsystem. The directional distribution of the radiative heat flux incident on the sample was modeled by Monte-Carlo ray-tracing method [14]. The spectral distribution is assumed equivalent to Planck's blackbody distribution at 5780 K, which corresponds to an approximation of the solar spectrum. Radiation incident on the upper surface of the sample undergoes absorption, reflection, and transmission. Thus, for the sample:

$$q''_{in} = q''_a + q''_{reflected} + q''_\tau \tag{11}$$

$$q''_\tau = \tau q''_{in} \tag{12}$$

$$q''_a = (q''_{in} - q''_\tau)(\varepsilon_{s,0-\lambda_1}F_{0-\lambda_1 T_{source}} + \varepsilon_{s,\lambda_1-\lambda_2}F_{\lambda_1 T_{src}-\lambda_2 T_{source}} + \cdots + \varepsilon_{s,\lambda_n-\infty}F_{\lambda_n T_{source}-\infty}) \tag{13}$$

where the gray band approximation of the hemispherical spectral emissivity has been employed. F denotes blackbody fractional function, $F_{\lambda_1 T-\lambda_2 T} = \frac{\int_{\lambda_1}^{\lambda_2} e_{\lambda b}(T)\,d\lambda}{\sigma T^4}$, with

$e_{\lambda b}$ being the blackbody spectral emissive power. Similarly, for the plate, neglecting transmission:

$$q''_{\text{in}} = q''_{\text{a}} + q''_{\text{reflected}} \tag{14}$$

$$q''_{\text{a}} = q''_{\text{in}}(\varepsilon_{\text{p},0-\lambda_1} F_{0-\lambda_1 T_{\text{source}}} + \varepsilon_{\text{p},\lambda_1-\lambda_2} F_{\lambda_1 T_{\text{source}}-\lambda_2 T_{\text{source}}} + \cdots + \varepsilon_{\text{p},\lambda_n-\infty} F_{\lambda_n T_{\text{source}}-\infty}) \tag{15}$$

The radiative flux emitted by the surface at T is

$$q''_{\text{e}} = \sigma T^4(\varepsilon_{0-\lambda_1} F_{0-\lambda_1 T} + \varepsilon_{\lambda_1-\lambda_2} F_{\lambda_1 T-\lambda_2 T} + \cdots + \varepsilon_{\lambda_n-\infty} F_{\lambda_n T-\infty}) \tag{16}$$

Inside the sample, the total heat flux has two components:

$$q''_{\text{total}} = (1-p)q''_{\text{c}} + pq''_{\text{r}} \tag{17}$$

where q''_{c} is the portion transferred by conduction, q''_{r} is the one transferred by radiation, and p designates the sample's porosity. Using Fourier's law, the conductive heat transfer through the sample is given by

$$q''_{\text{c}} = -k_{\text{c}} \nabla T \tag{18}$$

The radiative heat transfer inside the porous sample is determined assuming the Rosseland diffusion approximation for an optically thick medium [15]:

$$q''_{\text{r}} = -k_{\text{r}} \nabla T \tag{19}$$

where k_{r} is calculated using the gray band approximation by

$$k_{\text{r}} = -\frac{4}{3}\sigma T^3 \left\{ \frac{1}{K_{0-\lambda_1}} \left[4F_{0-\lambda_1 T} + \frac{15}{\pi^4} \frac{\zeta_1^3}{e^{\zeta_1}-1} \right] + \frac{1}{K_{\lambda_1-\lambda_2}} \left[4F_{\lambda_1 T-\lambda_2 T} + \frac{15}{\pi^4} \left(\frac{\zeta_2^3}{e^{\zeta_2}-1} - \frac{\zeta_1^3}{e^{\zeta_1}-1} \right) \right] + \cdots + \frac{1}{K_{\lambda_n-\infty}} \left[4F_{\lambda_n-\infty} - \frac{15}{\pi^4} \frac{\zeta_n^3}{e^{\zeta_n}-1} \right] \right\} \tag{20}$$

with $\zeta = C_2/\lambda T$.

Similarly, the total heat flux between the sample and plate at their interface is

$$q''_{\text{total,interface}} = (1 - p_{\text{interface}}) q''_{\text{interface}} + p_{\text{interface}} q''_{\text{r,interface}} \tag{21}$$

where $p_{\text{interface}}$ stands for the sample porosity at the interface zone, which is higher than the average porosity of the sample due to the particles' spherical shape. The heat transferred through the sample-plate interface is

$$q''_{\text{interface}} = h_{\text{interface}}(T_{\text{s,w}} - T_{\text{p,w}}) \tag{22}$$

The portion transferred by radiation through the pores at the sample-plate interface is

$$q''_{\text{r,interface}} = \frac{F_{0-\lambda_1 T_{\text{s,w}}} \sigma T_{\text{s,w}}^4 - F_{0-\lambda_1 T_{\text{p,w}}} \sigma T_{\text{p,w}}^4}{\frac{1}{\varepsilon_{\text{s},0-\lambda_1}} + \frac{1}{\varepsilon_{\text{p},0-\lambda_1}} - 1} + \frac{F_{\lambda_1 T_{\text{s,w}}-\lambda_2 T_{\text{s,w}}} \sigma T_{\text{s,w}}^4 - F_{\lambda_1 T_{\text{p,w}}-\lambda_2 T_{\text{p,w}}} \sigma T_{\text{p,w}}^4}{\frac{1}{\varepsilon_{\text{s},\lambda_1-\lambda_2}} + \frac{1}{\varepsilon_{\text{p},\lambda_1-\lambda_2}} - 1} + \cdots + \frac{F_{\lambda_n T_{\text{s,w}}-\infty} \sigma T_{\text{s,w}}^4 - F_{\lambda_n 1 T_{\text{p,w}}-\infty} \sigma T_{\text{p,w}}^4}{\frac{1}{\varepsilon_{\text{s},\lambda_n-\infty}} + \frac{1}{\varepsilon_{\text{p},\lambda_n-\infty}} - 1} \tag{23}$$

where $T_{\text{s,w}}$ and $T_{\text{p,w}}$ are the temperatures at the boundaries of the two materials. Computation of natural convection at the exposed surfaces of both sample and plate has been carried out using the following correlations [16]:

For horizontal surfaces ($L \equiv \frac{A}{P}$):

$$\overline{Nu}_L = 2.52 \quad \text{for } Ra_L < 10^4 \tag{24}$$

$$\overline{Nu}_L = 0.54 Ra_L^{\frac{1}{4}} \quad \text{for } 10^4 \leqslant Ra_L < 10^7 \tag{25}$$

$$\overline{Nu}_L = 0.15 Ra_L^{\frac{1}{3}} \quad \text{for } 10^7 \leqslant Ra_L < 10^{11} \tag{26}$$

For vertical surfaces ($L \equiv H$):

$$\overline{Nu}_L = \left[0.825 + \frac{0.387 Ra_L^{\frac{1}{6}}}{\left[1 + \left(\frac{0.492}{Pr} \right)^{\frac{9}{16}} \right]^{\frac{8}{27}}} \right]^2 \tag{27}$$

with properties of air evaluated at the average boundary layer temperature. The convective flux is then obtained from

$$q''_{\text{cv}} = \frac{\overline{Nu} \cdot k_{\text{c,air}}}{L} (T_{\text{w}} - T_{\infty}) \tag{28}$$

Finally, the energy sink due to chemistry in the sample is given by

$$q_{\text{ch}} = \Delta H_T^{\text{o}} \frac{\text{d}n_{\text{CaCO}_3}}{\text{d}t} = -\Delta H_T^{\text{o}} \frac{\text{d}x}{\text{d}t} n_{0,\text{CaCO}_3} \tag{29}$$

This term is set to zero in the plate.

5. Methodology

The finite volume method was employed for a discretized domain. Integration of Eq. (4) over the control volume Ω_j and time interval $\Delta t = t^{n+1} - t^n$ yields

$$\int_{t^n}^{t^{n+1}} \int_{\Omega_j} \frac{\partial U}{\partial t} \text{d}V \,\text{d}t = -\int_{t^n}^{t^{n+1}} \int_{\Omega_j} \nabla \cdot \vec{q}'' \,\text{d}V \,\text{d}t + \int_{t^n}^{t^{n+1}} \int_{\Omega_j} q''' \,\text{d}V \,\text{d}t \tag{30}$$

For Ω_j small and Δt short, ρ and c_p are constant. Substituting all terms in their discretized form and solving for T, yields

$$T_j^{n+1} = T_j^n + \frac{\Delta t}{\rho_j^n V_j c_{\mathrm{p},j}^n}\left(\sum_l \vec{q}''\Big|_l^n \cdot \vec{S}_l + q_j^n\right) \tag{31}$$

The heat fluxes through cell faces may be of radiative, convective, or conductive nature. They are evaluated at each time step n using the Eqs. (11)–(28). The solution begins by setting the initial conditions in the whole domain:

$$\begin{cases} T_\mathrm{s} = T_0 \\ T_\mathrm{p} = T_0 \end{cases} \tag{32}$$

The new temperature field is then computed using Eq. (31). Temperatures at boundaries are calculated as a function of the already computed heat fluxes and temperatures using Eqs. (5)–(10). For example, the temperature at t-face of cell Ω_j laying directly at the top surface of the sample is calculated using

$$T_{\mathrm{t}_j}^{n+1} = T_j^{n+1} + \frac{\Delta z}{2k_j^n} q''|_{\mathrm{t}_j}^n \tag{33}$$

where

$$k_j^n = (1-p)k_{\mathrm{c},j}^n + pk_{\mathrm{r},j}^n \tag{34}$$

and the net heat flux through the top face of cell j at time step n is

$$q''|_{\mathrm{t}_j}^n = q''_{\mathrm{cv}}|_{\mathrm{t}_j}^n + q''_{\mathrm{e}}|_{\mathrm{t}_j}^n - q''_{\mathrm{a}}|_{\mathrm{t}_j}^n \tag{35}$$

Since the material properties of sample and plate are functions of temperature, they are also evaluated at each time step. Further, the material properties of the sample are functions of its composition, which in turn changes with time. Thus, the ρ, c_p, k, and ε of cell Ω_j at time step n are, respectively:

Table 2
Baseline parameters used in the calculation

Parameter	Value	Unit
$C_{p,\mathrm{CaCO_3}}$ [a]	$104.52 + 21.92\mathrm{E}-3\cdot T - 2.59\mathrm{E}6\cdot T^{-2}$	$\mathrm{J\,mol^{-1}\,K^{-1}}$
$C_{p,\mathrm{CaO}}$ [a]	$50.42 + 4.18\mathrm{E}-3\cdot T - 0.85\mathrm{E}6\cdot T^{-2}$	$\mathrm{J\,mol^{-1}\,K^{-1}}$
$C_{p,\mathrm{SiC}}$ [b]	$0.85\cdot(10.997\cdot\ln(T) - 30.213)$	$\mathrm{J\,mol^{-1}\,K^{-1}}$
E_a [c]	187,300	$\mathrm{J\,mol^{-1}}$
g [d]	0.5	–
k_0 [c]	400,000	$\mathrm{s^{-1}}$
$k_{\mathrm{c,CaCO_3}}$ [e,f]	0.80	$\mathrm{W\,m^{-1}\,K^{-1}}$
$k_{\mathrm{c,CaO}}$ [e,f]	0.60	$\mathrm{W\,m^{-1}\,K^{-1}}$
$k_{\mathrm{c,SiC}}$ [e]	5.25	$\mathrm{W\,m^{-1}\,K^{-1}}$
K	350	$\mathrm{m^{-1}}$
p [c]	0.44	–
$p_\mathrm{interface}$	0.55	–
$\varepsilon_{\lambda,\mathrm{CaCO_3}}$ [g]	0.19 for $\lambda \leqslant \lambda_\mathrm{c}$, 0.81 for $\lambda > \lambda_\mathrm{c}$	–
$\varepsilon_{\lambda,\mathrm{CaO}}$ [g]	0.41 for $\lambda \leqslant \lambda_\mathrm{c}$, 0.59 for $\lambda > \lambda_\mathrm{c}$	–
$\varepsilon_{\mathrm{SiC}}$ [g]	0.75	–
λ_c [g]	2.4×10^{-6}	m
$\rho_{0,\mathrm{CaCO_3}}$ [c]	1400	$\mathrm{kg\,m^{-3}}$
ρ_{SiC} [c]	2700	$\mathrm{kg\,m^{-3}}$
τ	0.05	–

[a] Ref. [18].
[b] Ref. [20].
[c] Measured.
[d] Ref. [9].
[e] Ref. [19].
[f] Ref. [17].
[g] Ref. [21].

Table 3
Measured peak incident radiative flux at the focal plane, mean incident radiative flux over sample, and mean incident radiative flux over plate

Arc current A	Peak flux $\mathrm{W\,m^{-2}}$	Mean flux over sample $\mathrm{W\,m^{-2}}$	Mean flux over plate $\mathrm{W\,m^{-2}}$
200	665,875	550,084	146,760
300	1199,630	929,719	248,046

$$\rho_j^n = \frac{n_{\mathrm{CaCO_3}}\big|_j^n M_{\mathrm{CaCO_3}} + \left(n_{0,\mathrm{CaCO_3}}\big|_j^n - n_{\mathrm{CaCO_3}}\big|_j^n\right) M_{\mathrm{CaO}}}{V_j} \tag{36}$$

$$c_{\mathrm{p},j}^n = \frac{n_{\mathrm{CaCO_3}}\big|_j^n C_{p,\mathrm{CaCO_3}}\big|_j^n + \left(n_{0,\mathrm{CaCO_3}}\big|_j^n - n_{\mathrm{CaCO_3}}\big|_j^n\right) C_{\mathrm{CaO}}\big|_j^n}{\rho_j^n V_j} \tag{37}$$

$$k_{\mathrm{c},j}^n = \frac{k_{\mathrm{CaCO_3}}\big|_j^n n_{\mathrm{CaCO_3}}\big|_j^n M_{\mathrm{CaCO_3}} + k_{\mathrm{CaO}}\big|_j^n \left(n_{0,\mathrm{CaCO_3}}\big|_j^n - n_{\mathrm{CaCO_3}}\big|_j^n\right) M_{\mathrm{CaO}}}{\rho_j^n V_j} \tag{38}$$

$$\varepsilon_{\lambda,j}^n = \frac{\varepsilon_{\lambda,\mathrm{CaCO_3}}\big|_j^n n_{\mathrm{CaCO_3}}\big|_j^n M_{\mathrm{CaCO_3}} + \varepsilon_{\lambda,\mathrm{CaO}}\big|_j^n \left(n_{0,\mathrm{CaCO_3}}\big|_j^n - n_{\mathrm{CaCO_3}}\big|_j^n\right) M_{\mathrm{CaO}}}{\rho_j^n V_j} \tag{39}$$

The extinction coefficient K in the sample has been assumed to be constant with temperature and composition, i.e. same value for $CaCO_3$ and CaO. It is evaluated for scattering by large diffuse spheres as

$$K = a + \sigma_s = \pi R^2 N \tag{40}$$

where N is the number of particles of radius R per unit volume. Since N and R remain constant during the reaction,

$$N = \frac{3(1-p)}{4\pi R^3} \tag{41}$$

Substituting in Eq. (40),

$$K = \frac{3(1-p)}{4R} \tag{42}$$

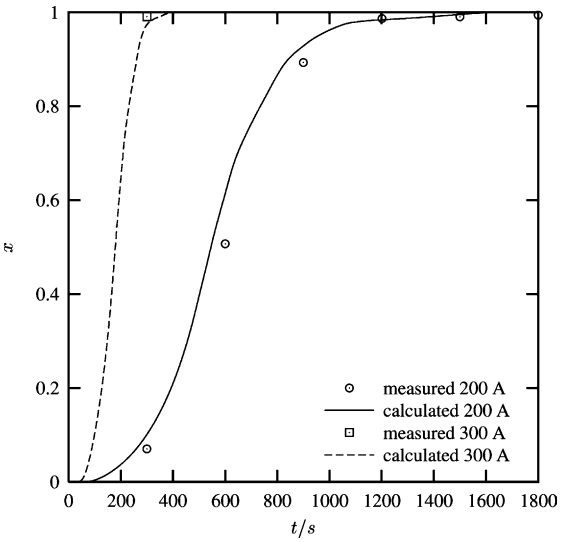

Fig. 4. Extent of the reaction as a function of time for arc currents 200 and 300 A: measured values (data points) and calculated curves.

Table 4
Relative error in the measurement of reaction extent x, and relative difference between calculated and measured values as a function of time for the run at 200 A

t/s	Error/%	$\lvert 1 - (x_{\mathrm{calculated}}/x_{\mathrm{measured}})\rvert$/%
300	19.89	43.08
600	2.76	21.01
1201	1.57	3.95
1500	1.42	0.30
1800	1.41	0.50

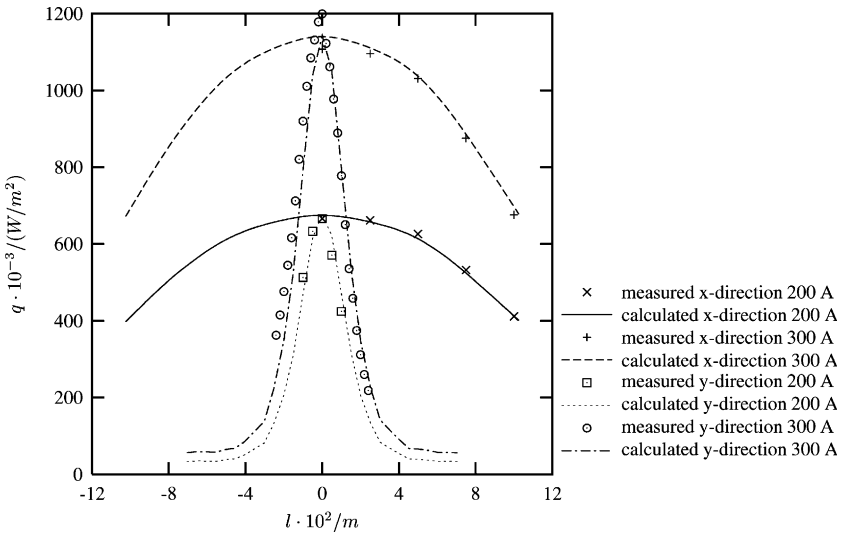

Fig. 3. Flux distribution across the x- and y-axis at the focal plane of the high-flux solar simulator for arc currents 200 and 300 A: optically measured values (data points) and calculated curves using Monte-Carlo ray tracing.

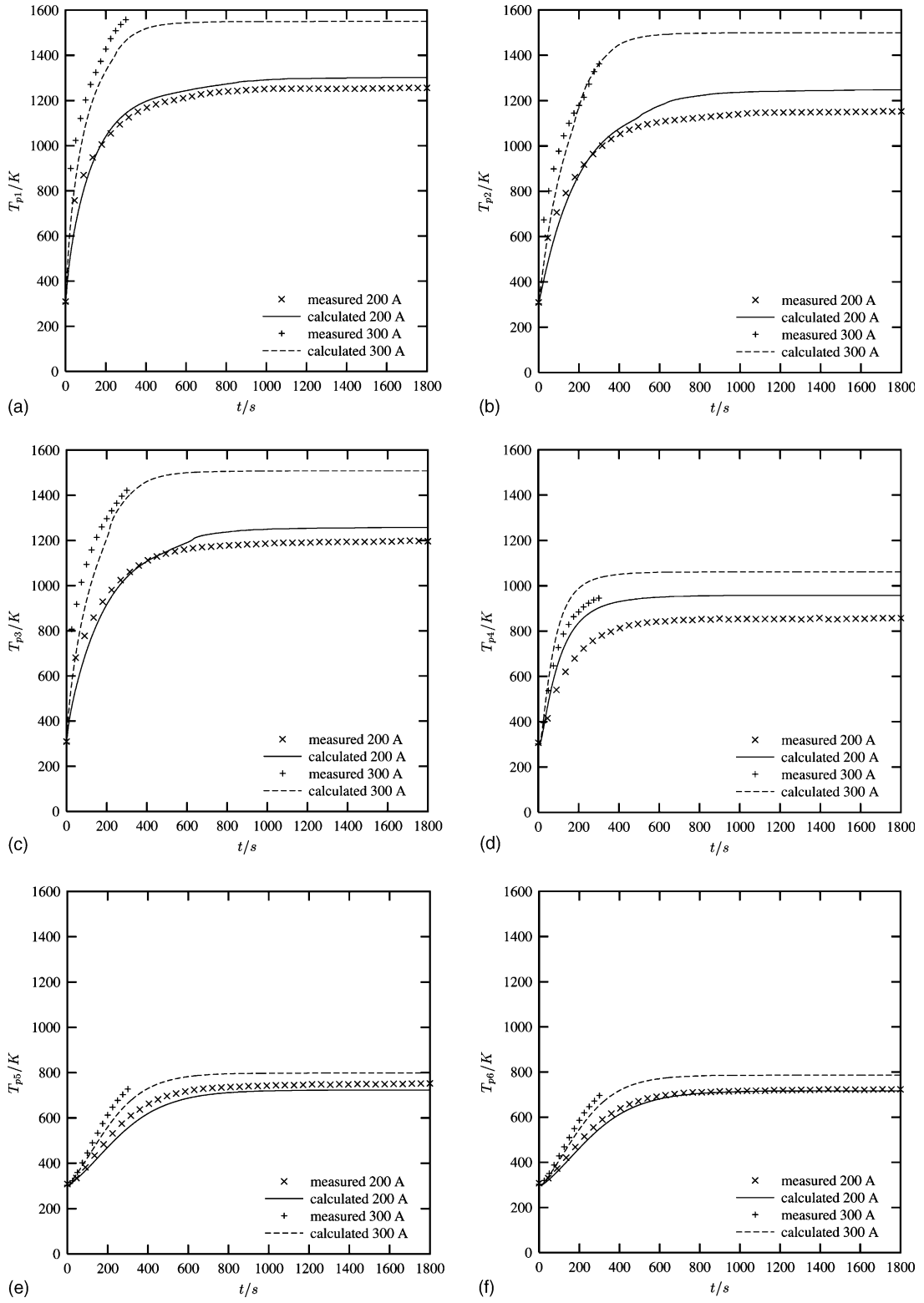

Fig. 5. Calculated and measured variation of temperatures with time for (a) T_{p1}, (b) T_{p2}, (c)T_{p3}, (d) T_{p4}, (e) T_{p5}, and (f) T_{p6}.

For a mean particle radius $R = 0.00125$ m and a porosity $p = 0.44$, $K = 336\ \mathrm{m}^{-1}$.

For the calculation of radiation and conduction fluxes across the cell boundaries, the mean k_c and k_r between adjacent cells are taken as $k^n_{c,j+\frac{1}{2}} = \frac{k^n_{c,j}+k^n_{c,j+1}}{2}$ and $k^n_{r,j+\frac{1}{2}} = \frac{k^n_{r,j}+k^n_{r,j+1}}{2}$.

6. Theoretical and experimental results

Table 2 shows the baseline parameters used in the calculation. Experimental runs were performed with arc currents of 200 and 300 A. The measured peak flux at the focal plane, mean flux over the sample, and mean flux over the plate are shown in Table 3. The calculated and measured power flux distributions at the focal plane, along the x and y directions, are shown in Fig. 3. The Monte-Carlo numerical results fit well to the measured values. A slight deviation and asymmetry lie within the error of the measurements. Fig. 4 shows the extent of the reaction as a function of time, measured and calculated. For the run at 200 A, the computed curve agrees well with the measured of the reaction, but differ by 43% at the beginning and 21% half way in the reaction progress ($x = 0.5$), where the reaction rate peaks. For the run at 300 A, the predicted curve agrees well with the single measurement. Table 4 lists the relative error in the measurement and the difference between calculated and measured values as a function of time for the run at 200 A.

The calculated and measured variations of temperatures with time at different plate locations are shown in Fig. 5 for runs at arc currents 200 and 300 A. In general, the agreement is reasonably good and Table 5 shows the relative difference between calculated and measured values at $x = 0.07$, 0.51, and 0.99 for the run at 200 A. The differences are believed to be mainly the result of discrepancies between the real material properties (C_p, k, and ε) of the actual experimental system and those employed in the modeled system that were extracted from the literature [17–21]. A sensitivity analysis revealed that the strongest temperature variation was observed when varying either the emissivities of both materials or the distribution of the incoming flux.

As far as heat losses from the system (sample + plate) to the environment are concerned, Fig. 6 shows the calculated time-dependent percentage of the incident power lost either by radiation (both emission and reflection) and by natural convection. As expected, the radiative losses are dominant and about six times higher than the convective ones.

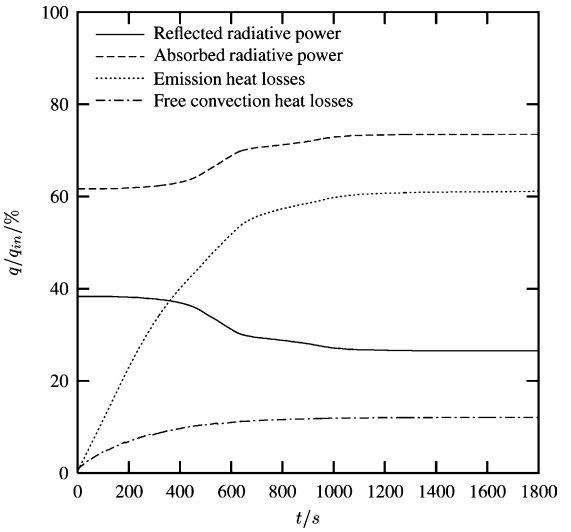

Fig. 6. Time-dependent energy losses from the system (sample + plate) to the environment.

7. Summary and conclusions

A transient 3D model that links thermal radiation, conduction, and natural convection heat transfer to the chemical reaction has been applied for limestone decomposition under direct irradiation. The model uses the Monte-Carlo ray-tracing technique for determining the radiative flux boundary conditions and the finite volume method for solving the unsteady energy equation coupled to the reaction kinetics. This model enables to treat a non-isothermal non-grey chemical system with a time-dependent chemical composition. The computed temperature field and reaction extent are in a good agreement with the experimentally measured values obtained with samples of limestone directly exposed to radiative fluxes. The heat transfer model can be applied in the treatment of transient problems involving solid reactants directly exposed to an external source of

Table 5
Relative difference $|1 - (T_{\mathrm{calculated}}/T_{\mathrm{measured}})|$, in %, between measured and calculated temperatures at various locations (see Table 1 and Fig. 2) as a function of the reaction extent for the run at 200 A

x	T_{p1}	T_{p2}	T_{p3}	T_{p4}	T_{p5}	T_{p6}
0.07	2.40	1.05	1.16	16.57	7.46	5.31
0.51	2.61	6.55	2.51	12.98	4.40	1.78
0.99	3.74	8.36	5.21	11.80	3.49	0.87

concentrated thermal radiation and undergoing heterogeneous thermochemical decomposition.

Acknowledgements

Financial support from the BFE—Swiss Federal Office of Energy and the BBW—Swiss Federal Office of Education and Science is gratefully acknowledged.

References

[1] T. Bergunge, M. Dauelsberg, L. Kadinski, Yu.N. Makarov, V.S. Yuferev, D. Schmitz, G. Strauch, H. Jürgensen, Process optimisation of MOVPE growth by numerical modelling of transport phenomena including thermal radiation, J. Crystal Growth 180 (1997) 660–669.

[2] E.I. Vitkin, V.G. Karelin, A.A. Kirillov, A.S. Suprun, Ju.V. Khadyka, A physico-mathematical model of rocket exhaust plumes, Int. J. Heat Mass Transfer 40 (1997) 1227–1241.

[3] K. Kudo, H. Taniguchi, K. Guo, T. Katayama, T. Nagata, Heat transfer simulation in a furnace for steam reformer, Kagaku Kogaku Ronbun. 17 (1991) 103–110.

[4] D. Vortmeyer, R. Stahl, Thermal radiation controlled ignition/extinction phenomena in a system of separated catalyst layers with exothermal chemical reaction, Chem. Eng. Sci. 36 (1981) 1373–1379.

[5] C.Y. Han, S.W. Baek, Radiative ignition of volatile gases on a vertical fuel plate, Combust. Sci. Technol. 109 (1995) 309–325.

[6] M.S. Liu, C.K. Choi, C.W. Leung, Startup analysis of oil-fired furnace—the smoothing Monte-Carlo model approach, Heat Mass Transfer 37 (2001) 449–457.

[7] A. Steinfeld, R. Palumbo, Solar thermochemical process technology, in: R.A. Meyers (Ed.), Encyclopedia of Physical Science and Technology, vol. 15, Academic Press, 2001, pp. 237–256.

[8] E.A. Fletcher, Solarthermal processing: a review, J. Solar Energy Eng. 123 (2001) 63–74.

[9] P.K. Gallagher, D.W. Johnson, The effects of sample size and heating rate on the kinetics of the thermal decomposition of $CaCO_3$, Thermochim. Acta 6 (1973) 67–83.

[10] B.V. L'vov, The physical approach to the interpretation of the kinetics and mechanism of thermal decomposition of solids: the state of the art, Thermochim. Acta 373 (2001) 97–124.

[11] B.V. L'vov, L.K. Polzik, V.L. Ugolkov, Decomposition kinetics of calcite: a new approach to the old problem, Thermochim. Acta 390 (2002) 5–19.

[12] D. Hirsch, P.v. Zedtwitz, T. Osinga, J. Kinamore, A. Steinfeld, A new 75 kW high-flux solar simulator for high-temperature thermal and thermochemical research, ASME—J. Solar Energy Eng. 125 (2003) 117–120.

[13] C. Hirsch, Numerical Computation of Internal and External Flows, Fundamentals of Numerical Discretization, vol. 1, John Wiley & Sons, 1997, pp. 237–260.

[14] J. Petrasch, Diploma Thesis, Swiss Federal Institute of Technology, Zürich, 2001.

[15] R. Siegel, J.R. Howell, Thermal Radiation Heat Transfer, third ed., Hemispere Publishing Company, Washington, DC, 1992, pp. 751–754.

[16] F.P. Incropera, D.P. DeWitt, Introduction to Heat Transfer, third ed., John Willey &Sons, 1996, pp. 456–463.

[17] J.A. Oates, Lime and Limestone, Chemistry and Technology, Production and Uses, WILEY-VCH, Weinheim, 1998, pp. 18–20, 117–119.

[18] M. Binnewies, E. Milke, Thermochemical Data of Elements and Compounds, second ed., WILEY-VCH, Weinheim, 2002, pp. 230, 251, 254, 287.

[19] Y.S. Touloukian, R.W. Powell, C.Y. Ho, P.G. Klemens, Thermophysical Properties of Matter, Thermal Conductivity, Nonmetallic Solids, vol. 2, IFI/Plenum, New York, Washington, 1970, pp. 141, 585, 759.

[20] Y.S. Touloukian, E.H. Buyco, Thermophysical Properties of Matter, Specific Heat, Nonmetallic Solids, vol. 5, IFI/Plenum, New York, Washington, 1970, pp. 57–59, 448–450, 1112–1114.

[21] Y.S. Touloukian, D.P. De Witt, Thermophysical Properties of Matter, Thermal Radiative Properties, Nonmetallic Solids, vol. 8, IFI/Plenum, New York, Washington, 1972, pp. 218–224, 583–586, 791–810.